Imaging of dynamic processes in materials with a laser-wakefield accelerator

J. Kang,[1] R.J. Shalloo[2] M.J. Higgins,[3] S.J.D. Dann,[4] J.-N. Gruse,[5] C.I.D. Underwood,[6]
A.F. Antoine,[7] C. Arran,[6,8,9] C.D. Baird,[4] M.D. Balcazar,[7] N. Bourgeois,[4] J.A. Cardarelli,[7]
K. Krushelnick,[7] S.P.D. Mangles,[5] C.D. Murphy,[6] N. Lu,[3] P.P. Rajeev,[4] M.P. Selwood,[6]
D.R. Symes,[4] C.P. Ridgers,[6] A.G.R. Thomas,[7] C. Thornton,[4] Z. Najmudin,[5] P.G. Sanders,[10]
P.D. Staublin,[3] A.J. Shahani[1,3,*] and M.J.V. Streeter[11,†]

[1]*Department of Chemical Engineering, University of Michigan, Ann Arbor, Michigan 48109, USA*
[2]*Deutsches Elektronen-Synchrotron DESY, Notkestr. 85, 22607 Hamburg, Germany*
[3]*Department of Materials Science and Engineering, University of Michigan, Ann Arbor, Michigan 48019, USA*
[4]*Central Laser Facility, STFC Rutherford Appleton Laboratory, Didcot OX11 0QX, United Kingdom*
[5]*The John Adams Institute for Accelerator Science, Imperial College London, London SW7 2BZ, United Kingdom*
[6]*York Plasma Institute, School of Physics, Engineering and Technology, University of York, York YO10 5DD,
United Kingdom*
[7]*Center for Ultrafast Optical Science, University of Michigan, Ann Arbor, Michigan 48109-2099, USA*
[8]*Physics Department, Lancaster University, Lancaster LA1 4YB, United Kingdom*
[9]*The Cockcroft Institute, Keckwick Lane, Daresbury WA4 4AD, United Kingdom*
[10]*Department of Materials Science and Engineering, Michigan Technological University, Houghton,
Michigan 49931, USA*
[11]*Centre for Light-Matter Interactions, School of Maths and Physics, Queen's University, Belfast,
Belfast BT7 1NN, United Kingdom*

Betatron x rays generated from laser-wakefield accelerators are a promising source for imaging dynamic processes in materials. Here, we present proof-of-concept imaging of microstructural evolution in a hyper-monotectic Al-Bi alloy, which consists of liquid Bi particles in a solid Al matrix. The images capture the elongation and fragmentation of Bi particles upon isothermal annealing. Because of the femtosecond time scale of the betatron source, the images are not subject to motion blur, whereas the accessibility of the source allows for studies of long-term processes such as annealing. The high-resolution data reveal that the evolution of Bi particles is mediated by an interplay of grain-boundary wetting and morphological instability, in stark contrast to an earlier proposal for (inverse) coarsening.

Understanding the evolution of microstructure in material processes is key to controlling it. To this end, x-ray imaging offers unique opportunities in nondestructive materials diagnostics during processing and service. X rays can penetrate deeply into materials and provide rich information from different interactions with matter, e.g., absorption [1,2], scattering [3,4], diffraction [5,6], and refraction [7,8]. With the aid of x-ray imaging techniques, we can measure unambiguously time-dependent properties and kinetics via *in situ* experiments. Recent examples include the migration of grain boundaries (GBs) with respect to GB curvature [9,10], the formation of porosity during laser-aided additive manufacturing [2,11], and the emergence of bulk grains during recrystallization [12].

Here, we look to take this concept further by using a new and accessible x-ray source to investigate the stability of a semisolid alloy during annealing. X-ray imaging can be implemented with different sources [13–17]. To date, real-time studies of microstructure evolution have relied on conventional synchrotron sources that provide a high photon flux. However, because of the limited accessibility of such facilities, there is strong motivation to translate the capabilities of conventional synchrotrons to compact x-ray sources. For example, a resolution of ~ 10 μm with an exposure time of ~ 1 s for the acquisition of

---

*Contact author: shahani@umich.edu
†Contact author: m.streeter@qub.ac.uk

a single absorption-contrast image can be accomplished using a liquid-metal-jet x-ray source [17]. Advancements in conventional tungsten-anode targets enable submicrometer resolution with a similar exposure time on the order of 1–10 s for single-image acquisition [18,19]. However, these sources suffer from a compromised spatial resolution and signal-to-noise ratio when the exposure time is reduced [20,21]. Thus, challenges remain in attaining capabilities comparable to those of conventional synchrotron sources.

The laser-wakefield accelerator (LWFA) has been intensively investigated to produce giga-electron-volt-range electron beams in centimeter-scale gas plasmas using commercially available ~ 100 TW lasers. The ultrashort laser pulse (tens of femtoseconds) used for the LWFA is focused, typically, to a spot size of a few tens of micrometers and drives a plasma wave with a phase velocity close to the speed of light. The strong electromagnetic fields generated by the plasma wave allow for the acceleration of electrons to relativistic energies. During the acceleration process, electrons oscillate in the strong focusing fields of the wakefield, resulting in the emission of betatron x rays in the energy range of 1–100 keV, with a pulse duration on the order of ten femtoseconds. LWFA betatron sources have demonstrated micrometer-scale source size [22,23], allowing phase-contrast-enhanced x radiography [24] of objects with micrometer-scale features. Experiments have also shown enhanced x-ray yield by using tailored plasma density profiles [25,26] and higher laser energies [27,28] (~ 10 J), obtaining up to $\sim 10^{10}$ photons per pulse (for photon energies > 5 keV). Thus, LWFA betatron sources can provide average spectral brightness comparable to those of micro-computed tomography machines and peak spectral brightness comparable to third-generation light sources ($\sim 10^{23}$ photons s^{-1} mm^{-2} mrad^{-2} per 0.1% bandwidth), such that this source holds great promise for imaging applications, including materials diagnostics [29,30].

In this work, we make use of the advantages of LWFA betatron x rays to probe the dynamic behavior of materials during the process of annealing. We focus on imaging the evolution of microstructure in a hypermonotectic Al-Bi alloy, which consists of immiscible and soft Bi particles in a harder Al matrix. This material is of particular interest because it is a promising candidate for automotive bearing applications [31–33]. It is also an appropriate choice for x-ray projection microscopy (x radiography) because of the large difference in attenuation between Al and Bi.

In general, a homogeneous dispersion of solid Bi particles will flow easily under sliding environments, resulting in a favorable tribological performance [34]. Unfortunately, due to the large density difference between Al and Bi, it is notoriously difficult to produce a uniform distribution of particles in conventional casting [35]. This is due to severe sedimentation and segregation of the heavier Bi

phase during solidification. To attain a redistribution of Bi particles, researchers have proposed a thermomechanical processing route for the solidified material [36]. During plastic deformation, the particles can redistribute through elongation and further fragmentation [36,37], although the exact mechanism remains an open question. One hypothesis is that small, misfitting particles may grow at the expense of large ones through inverse coarsening [38] provided that the increase in surface area (and hence surface free energy) is compensated for by the decrease in total elastic energy.

Here, we show that the process is instead mediated by grain-boundary wetting (GBW) followed by Rayleigh instability, leading to the breakdown of large particles into small particles. It should be emphasized that we investigate the microstructural dynamics above the melting temperature of the Bi phase (271.4 °C), in order to isolate the effect of stored elastic energy. Our efforts were made possible by new developments in real-time imaging with LWFA. Because of the femtosecond time scale of the betatron source, the single-shot images are not marred by motion blur [15]. This enables us to identify micrometer-scale particles and track their morphological evolution with high precision.

The experiment was carried out using the Gemini TA2 Ti:sapphire laser system at the Central Laser Facility at Rutherford Appleton Laboratory (RAL), using the same LWFA setup as reported in Shalloo *et al.* [39]. An illustration of the experimental layout for x radiography is given in Fig. 1. The 5-Hz laser pulses each contained 225 mJ in a pulse length of 45 fs and were focused with an $f/18$ off-axis parabolic mirror to $1/e^2$ spot radius of 16 μm, giving an in-vacuum peak normalized vector potential $a_0 = 0.55$. The gas cell was filled with a mixture of 5% nitrogen in helium, which was ionized by the driving laser pulse to a plasma electron number density of
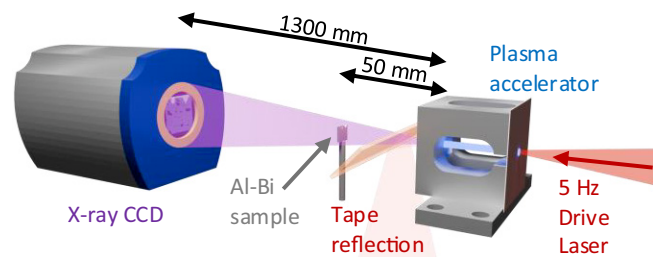

FIG. 1. An illustration of the experimental setup for x radiography using a laser-wakefield accelerator. The laser focus was aligned to the entrance of a 4-mm-long gas cell to drive the laser-wakefield accelerator. At the exit of the LWFA, a refreshable 25.4-μm-thick polyimide tape was used to divert the residual laser pulse, while the x rays passed through the Al-Bi sample and were detected by an x-ray CCD. The accelerated electron beams were deflected away from the x-ray CCD by a magnetic dipole placed 570 mm behind the gas cell.

$(1.8 \pm 0.3) \times 10^{19}$ cm^{-3}. Upon exiting the plasma accelerator, the residual laser is deflected away by a polyimide tape, while the betatron x rays pass through the sample onto the direct-detection x-ray CCD (Andor iKon-M 934 BR-DD), which was mounted onto the vacuum chamber.

An optical filter made up of a 200-nm Al coating on a 12.8-µm Mylar film was placed in front of the x-ray CCD to shield the diagnostic from optical background light and plasma emission. The x-ray beam was spectrally characterized (without the sample in place) by measuring the relative transmission through a multielement filter array and fitting a synchrotronlike spectrum, of the form $d^2I/dEd\Omega \propto \tilde{E}K_{2/3}^2(\tilde{E})$, where $\hat{E} = E/2E_c$ is the photon energy normalized to the critical energy E_c, and K is the modified Bessel function of the second kind. The camera counts were then converted to photon flux by accounting for the energy-dependent detector efficiency and the transmission of the light shielding (12.8-µm-thick Mylar and 600-nm-thick aluminum). A representative image and retrieved spectrum from the x-ray spectrum characterization is shown in Appendix A. For the series of shots reported in this paper, the critical frequency of the retrieved spectrum was (2.8 ± 0.7) keV, with a median $(1.5 \pm 0.3) \times 10^4$ photons mrad^{-2} above 1 keV.

For the experiment, we investigated an extruded Al-Bi alloy (with 20 wt % Bi) sample (see Appendix B for details on its preparation). The betatron x rays diverged from a source at the exit of the plasma, with the source-to-sample distance of 53 mm and source-to-detector distance of 1300 mm, resulting in a geometrical magnification of $M = 24.5$. The CCD had pixels of size 13×13 µm^2, and so the detector limit for the image resolution was 0.53 µm. Part of the residual LWFA electron beam also passed through the sample, generating background via bremsstrahlung. This background signal was uniformly distributed over the detector and was approximately 7% of the betatron signal. We imaged this sample in an interrupted *in situ* manner [5,16] by isothermally annealing it at 280 °C and then air quenching it after 0, 2, 4, 6, and 12 h. As noted previously, 280 °C is above the melting point of Bi; thus, Bi particles exist in the form of melt pools within the Al matrix phase over the course of the anneal.

We screened the as-collected or "raw" x-radiography images produced by each pulse of the LWFA based on the average counts on the x-ray CCD detector. For images above a set threshold, we conducted a series of normalizations, alignments, and transformations to combine them into a single low-noise image for each time step (see the information in Appendix C for further details). The spatial resolution of the resulting images was characterized using the Fourier-based power spectral density (PSD) [40] and found to be $x_{res} = 2\pi/k_{res} = 8.5$ µm. Thus, a few-micron-scale spatial resolution can be achieved using LWFA betatron x rays, in agreement with a previous report [15]. These images were recorded with an extremely short exposure time on the order of femtoseconds [24,41], which ensures that the images are free from motion blur, unlike conventional synchrotron-based imaging [13,42,43]. More specifically, during imaging at the synchrotron beamline, the relative sample-to-detector location can fluctuate at an amplitude of up to 0.5 µm due to vibration, leading to blurring of the images over the millisecond exposure time [15]. However, single-shot LWFA is much less likely to suffer from the same issue due to the ultrashort x-ray pulse, which allows visibility of the smallest Bi particles ($< x_{res}$ in size).

To track the same particle across time steps (provided it does not disappear completely during annealing), we invoked the Kuhn-Munkres algorithm [44–46]. This method solves the assignment problem by matching particles from one time step to the next by taking into consideration the particle size and location. That is, features of similar size and location identify the same particle across time steps. Figure 2 shows radiographs of the sample at different stages during the anneal. It can be seen that particles become thinner rather than more isotropic or circular in shape. The elongation of the particles in the horizontal direction of the field of view reflects the processing history, namely, plastic deformation (see Appendix B). Apparently, this morphological evolution cannot be attributed to (inverse) coarsening: the Al-Bi interfaces with high curvature do not recede over time, giving rise to a more rounded particle morphology, as would be predicted by coarsening theory [47]. The two largest visible particles [see the white arrows in Fig. 2(b) and an enlarged view for one of the particles in Fig. 2(e)] are further analyzed in Fig. 3.

As a characteristic length scale, we consider here the minor-axis length of an ellipse, representing the shortest diameter of the particle. Further evidence against coarsening theory comes from the fact that all size classes of particles show a decrease in minor-axis length over time according to Fig. 3(a), i.e., competitive growth does not apply. If it did, then we should see a crossover with the zero axis for a critical particle size [48,49].

Since Al and Bi are mutually insoluble and the mass of Bi is conserved, we postulate that: (i) the decrease in minor-axis length is offset by a corresponding increase in major-axis length; and (ii) this shape change is realized through a GBW process. If we accept (ii) for the moment, it follows that the tip of the wetting phase is ~ 1 µm thick based on past reports [50–52], and hence we are unable to measure reliably the major-axis length of the particles at the spatial resolution x_{res} of our images (i.e., the actual major-axis length is likely greater than that perceived). It can also be seen in Fig. 2(e) that, at the longest times (12 h), the thin Bi particles eventually break down into smaller ones, for reasons that will be discussed later.

Of course, the essential prerequisite for GBW is that the particles are situated on a GB rather than in the intragranular region. That is, the major axis of the ellipsoidal particles should follow the trace of the GB. To link the features seen
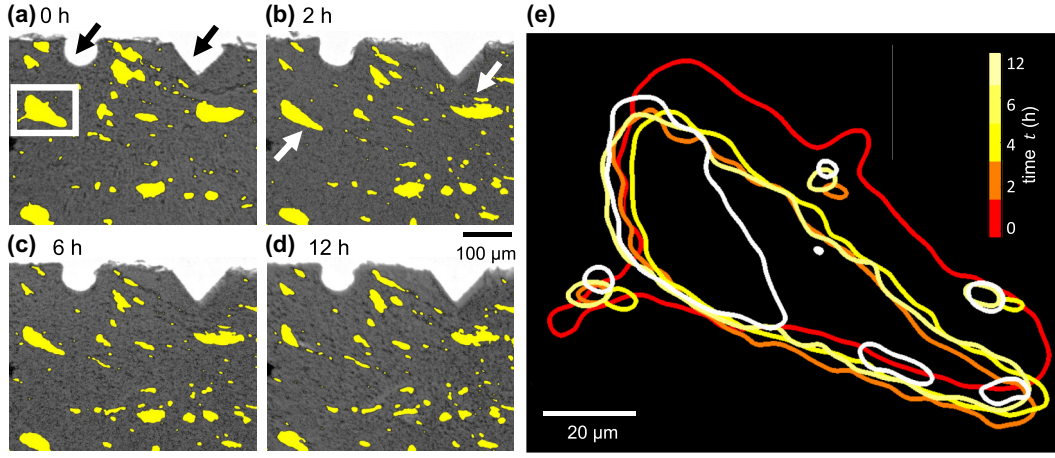
FIG. 2. Al-Bi sample imaged by x radiography using LWFA. (a)–(d) Registered and segmented images of the sample after (a) 0 h, (b) 2 h, (c) 6 h, and (d) 12 h of isothermal annealing at 280 °C. The yellow-colored regions represent segmented Bi particles; the grey regions are the Al matrix. The two arrows in panel (a) point to the fiducial markers, while those in panel (b) point to the largest particles in the field of view. (e) An enlargement of one of these particles [boxed in panel (a)] that fragments during annealing.

in x radiography with the underlying grain structure, we obtained crystallographic information on a sample from the same ingot via electron backscatter diffraction (EBSD) in a scanning electron microscope (SEM). In the resulting image, shown in Fig. 4, all Bi particles were observed to sit on GBs or their trijunctions, which provide capillary channels for GBW to occur.

Based on our time-resolved data, we can test the predictions of GBW theory. Among the different mechanisms proposed in the literature [50,53,54], it is clear that the imbalance between the grain boundary and the surface tensions of the solid and liquid plays a dominant role. According to a model by Glickman and Nathan [54], this imbalance creates a force at the root of the GB groove that causes stress-driven self-diffusion into the GB channel. By assuming that the GB acts as a perfect sink, and introducing a "dynamic" dihedral contact angle, they derived a constant wetting velocity, Γ, which depends on the GB diffusivity, the diffusion coefficient of one metal (here, Al) in the other (Bi), and the surface tensions of the GB and solid-liquid interface.

We interpret our time-resolved data in the framework of the aforementioned model. To do so, we assume the geometry shown in the inset in Fig. 3(b): the GB runs through the major axis of the ellipsoidal particle, such that wetting proceeds from both its vertices in the major-axis direction. Note again that the liquid-phase channel width is typically on the order of 1 μm [50–52,55], and so we are unable to directly measure the major-axis length or its rate of change over time (and hence the wetting velocity, Γ). Instead, we examine the thinning velocity along the minor axis, exploiting the fact that the volume of the liquid phase is conserved during GBW.

In this case, it can be shown that the kinetics are parabolic (see Appendix G). That is, the minor-axis length

L_{minor} varies with time t as

$$L_{\mathrm{minor}}(t) = (k_1 t + k_2)^{-1/2} + k_3, \tag{1}$$

where k_1, k_2, and k_3 are fitting parameters with physical significance. The positive constant k_1 is related to the wetting velocity Γ from Ref. [54] as $k_1 = 2\Gamma(2\pi/3\Omega)$, where Ω is the particle volume. Meanwhile, k_2 and k_3 account for the initial and final conditions and must also be positive. In the limit of long times, the asymptote $L_{\mathrm{minor}}(t \to \infty) = k_3$ reflects a Rayleigh instability [47], by which the particle will subdivide into smaller particles when the minor-axis length, L_{minor}, falls below the critical wavelength k_3. Indeed, we observe in Fig. 2(e) the fragmentation of particles at long times. Initially, $L_{\mathrm{minor}}(t = 0) = k_2^{-1/2} + k_3 \leq l$, where the latter inequality places a constraint on the fit of Eq. (1) to our data: the length L_{minor} cannot exceed the sample thickness ($l = 40$ μm).

We fit Eq. (1) to the measured data, allowing us to solve for k_1, k_2, and k_3. We examine specifically the two largest Bi particles [see the arrows in Fig. 2(b)] for which the minor-axis length can be faithfully obtained. Figure 3(b) demonstrates the goodness of fit. Of note is that data from the 12-h mark are not included here. This is because the liquid Bi pools started to fragment, signifying the end of GBW. At this stage, we postulate that the length of Bi pools exceeds the critical length for Rayleigh instability, resulting in fragmentation into smaller pools aligned with the GB trace. In the idealized transition from rod-shaped particles to spherical particles, the critical wavelength [56], λ^*, of the Rayleigh instability (in the kinetic limit) can be expressed as $2\sqrt{2}\,\pi L_{\mathrm{minor}}$ [47]. Employing this criterion, we calculate the critical minor-axis length at which the particle is expected to subdivide as 23.6 μm. Comparing our
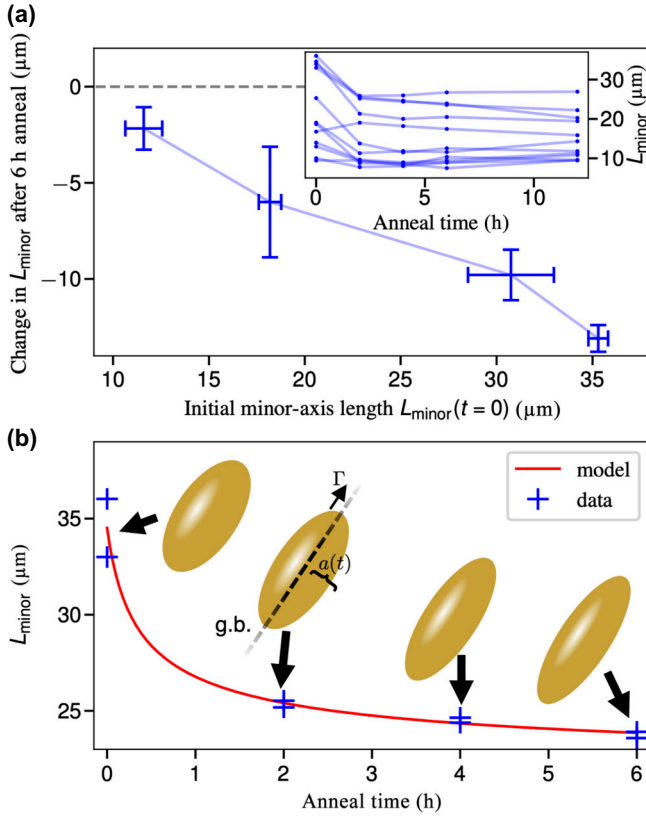
FIG. 3. Evolution of minor-axis length L_{minor}. (a) Relation between the particle's initial length and its change in length upon annealing. Data reflect 12 representative Bi particles over a period of 6 h. The error bars show the standard error of the data clusters. The inset shows the trajectories over time of the individual particles. (b) Discretized data on the two particles of interest, fit to a GBW model (red). The insets provide snapshots of the idealized particle evolution together with the model parameters (see text for details).
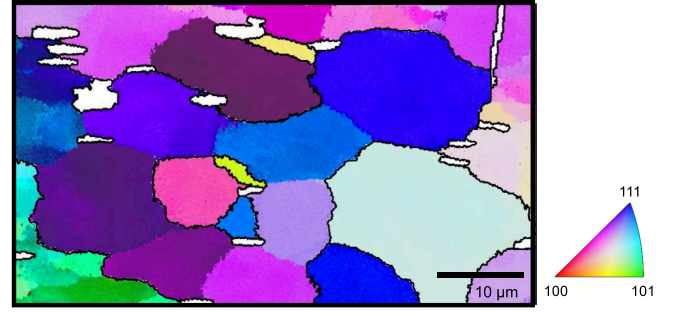

FIG. 4. SEM-EBSD image that shows Bi-particle distribution on the surface of a polished Al-Bi sample, together with the underlying Al grain structure. The white-colored regions represent Bi particles; the colored regions represent grain orientations with respect to the normal to the plane (see standard triangle).

calculation to the fitted model [Fig. 3(b)], we find a reasonable agreement with the fitting result of $L_{\mathrm{minor}}(t \to \infty) = k_3 = 19.6$ µm. The correct order of magnitude strongly suggests the transition of the governing dynamics from GBW to Rayleigh instability.

From the nonlinear regression, we find also $k_1 = 0.0165$ µm^2/h and therefore $\Gamma = 0.0636$ µm/s. We further validate our measured Γ by calculating it directly from the theoretical model, using the thermophysical parameters listed in Table I in Appendix F. It should be noted that there exist multiple references for the GB diffusivity as well as the activation enthalpy of lattice diffusion in Al [57,58], leading to a range of wetting velocities. Even so, we find good agreement between the wetting velocity calculated from tabulated parameters ($\Gamma = 0.0897$ to 0.00244 µm/s) and the value obtained from our measurements ($\Gamma = 0.0636$ µm/s). This implies that, at the early stages of annealing prior to morphological instability, the evolution of liquid Bi can be ascribed to a GBW process.

Our findings propose an original mechanism for the redistribution of large immiscible particles into smaller ones, through an interplay of GBW and morphological instability. Importantly, stored elastic strain is not the operant driving force. We expect that our results may pave the way toward a simple and general method to manufacture particle-containing alloys without deformation. Our processing strategy is especially amenable to a range of hypermonotectic alloys that contain soft particles, such as Al-In, where In is the particle phase. In such materials, GBW may occur even below the melting point T_M of the particles due to impurity or curvature depressions of T_M. For example, if the Bi particle is of the size ~ 10 nm, then T_M is $\sim 1\,°C$ less than in the bulk thermodynamic limit.

Our results also highlight the exciting opportunity for betatron x rays from LWFA to probe the dynamic processes of materials. They extend the potential of laser-based sources in different materials applications that require real-time monitoring, including, but not limited to, metal additive manufacturing (AM) as recently explored by Senthilkumaran *et al.* [30]. In recent years, AM has drawn worldwide attention as an emerging process for making complex three-dimensional objects. A central issue is to understand the flow in and around the melt pool as the powder bed is melted [1], which bears some superficial similarity to the behavior of liquid Bi pools in our work. Unfortunately, the design principles for AM are far from clear, as *post mortem* approaches are incapable of tracking the real-time evolution of microstructures.

The increasing accessibility of LWFA sources, compared to synchrotrons, allowed our study to follow several competing dynamic processes over more than 12 h. Deploying an LWFA source connected to an AM system would allow for real-time *in situ* imaging during AM builds to probe rapid solidification dynamics, melt-pool behavior, and powder redistribution during metal AM processes. Also, the ongoing development of ≥ 1-kHz-repetition-rate high-power laser systems, e.g., Ref. [59],

will enable studies of dynamic processes with ≤ 1 ms interframe durations. To this end, betatron x rays from LWFA can help meet the burgeoning need for direct imaging of microstructure evolution. Extending our approach to higher-power laser systems [60] will also enable submicron-resolution x radiography using plasma acceleration, further increasing its utility in materials science.

DATA AVAILABILITY

The data that support the findings of this article are openly available [61].

APPENDIX A: X-RAY SPECTRUM CHARACTERIZATION

The x-ray source was spectrally characterized in a series of shots with a multielement filter placed between the x-ray source and the detector. The relative transmission of the different elements of the filter could then be used to fit the free parameters of a given spectral shape. A synchrotronlike spectrum of the form $\mathrm{d}^2 I/\mathrm{d}E\mathrm{d}\Omega \propto \tilde{E}K_{2/3}^2(\tilde{E})$ was assumed, where $\hat{E} = E/2E_c$ is the photon energy normalized to the critical energy E_c, and K is the modified Bessel function of the second kind. An example camera image from the spectral calibration along with retrieved x-ray spectra are shown in Fig. 5.

APPENDIX B: PREPARATION OF MATERIALS

Ingots of Al-Bi alloy with a nominal composition containing 20 wt% Bi were cast at Michigan Technological University. The ingots were cast by melting 99.99% pure Al and Bi in a vacuum induction melt chamber under a controlled atmosphere. A vacuum of 10^{-4} Torr was achieved prior to heating. During heating, the chamber was backfilled to 680 Torr with 5.0 ultrahigh-purity argon, and then the alloy was melted. A permanent mold (gray iron)
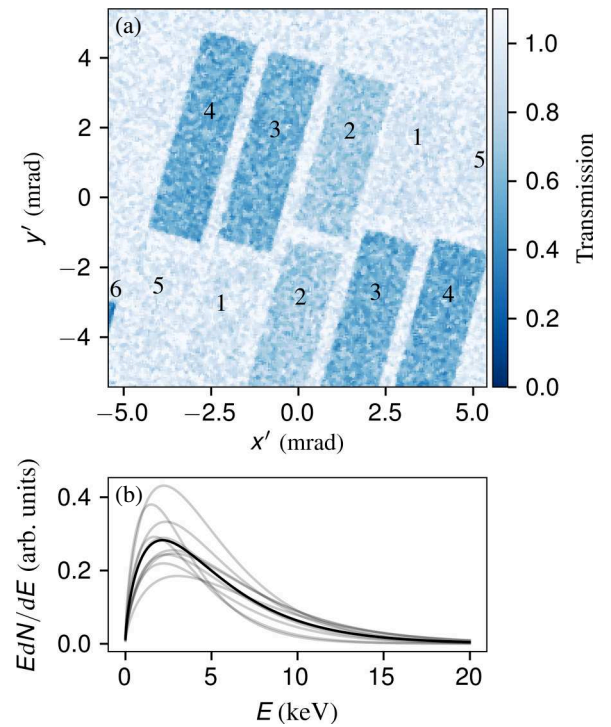

FIG. 5.   (a) X-ray transmission of the filter array for a single shot. The numeric labels in the image indicate the filter types, which are: 1, 21.85 ± 0.25 μm Mylar; 2, 20.15 ± 0.45 μm Mg; 3, 29.5 ± 0.3 μm Al-Mg (95%-5%); 4, 33.5 ± 1.1 μm Al-Mg-Si (98%-1%-1%); 5, 12.9 ± 0.1 μm Kapton; and 6, 50 μm W. (b) Plots of the retrieved x-ray spectra for 10 consecutive shots (grey) with nominally identical conditions and their average (black).

with bottom fill design was used to cast two 19×150 mm^2 rod ingots. The ingot was pre-annealed at 640 °C for 24 h in order to yield (i) an initial particle size above the spatial resolution limit of 8.5 μm for our x-ray imaging system and (ii) a sufficiently high particle number density to calculate robust statistics on the particle distribution (see below).

The subsequent material processing steps were loosely based on the prior work of Zha *et al.* [36], wherein severe plastic deformation and further annealing stimulate a redispersion of the Bi particles in the Al-Bi alloy. First, the solidified sample was deformed in a 110° equal channel angular extrusion die for 10 passes, employing the B_c route at ambient temperature [20,62]. Next, the deformed sample was machined via electric discharge machining and then mechanically polished in the shape of a lift-out grid of thickness ~ 40 μm to ensure acceptable transmission for the x-ray radiography experiments (i.e., at 5 keV, the transmission of Al and Bi is 0.1 and 10^{-3}, respectively). Finally, two fiducial markers (see half-circle and triangle in Fig. 2) were introduced using a focused ion beam (FIB) to aid alignment of the imaged field of view in consecutive x-ray radiography experiments. Annealing of the sample
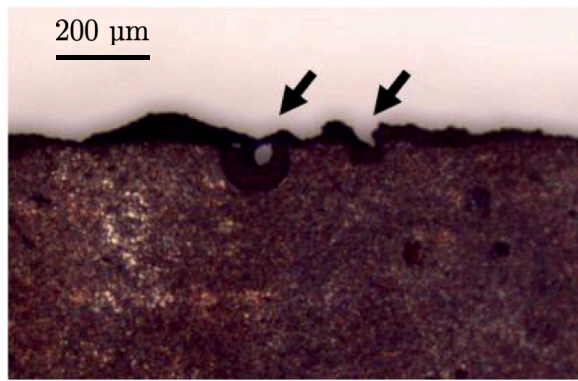
FIG. 6. Optical micrograph that shows the fiducial markers (see arrows) on the edge of a sample. The two markers are in the shape of a circle and square.

was done with a muffle furnace, which provided uniform heating through the embedded ceramic fiber insulation.

Figure 6 provides a closer view of the fiducial markers, albeit on a different sample. The sample imaged in Fig. 2 is prepared in the same manner but with different marker shapes (half-circle and triangle). A thermally grown oxide "skin" protected the Al-Bi microstructure during semisolid processing and handling.

APPENDIX C: IMAGE PROCESSING

Figure 7 summarizes the image processing procedure. We registered the images through an affine transformation (translation and shear) based on the projected locations and geometries of the two fiducial markers (half-circle and triangle). Shear accounted for the fact that the sample may have tilted during mounting in the interrupted anneal schedule. After registration, we filtered and binarized the images into two classes (Bi particles and Al matrix). Nonlinear diffusion of the Perona-Malik type [63] helped to suppress low-frequency "speckle" noise while preserving semantically important Al-Bi interfaces. Even so, binarization or segmentation left some small ($\leq 10 \ \mu m^2$) particles invisible. This is not too problematic because we focus on particles with a larger size that provide a more reliable measurement of the morphological evolution. To measure particle size, we applied morphological opening for those particles that have low convexity [16], defined as the ratio of particle perimeter to that of the convex hull. This was done to prevent us from overestimating the particle size (namely, the minor-axis length) due to small protrusions on the surfaces of the particles.

APPENDIX D: ELECTRON BACKSCATTER DIFFRACTION MEASUREMENTS

The positions of the Bi particles relative to the underlying Al grain structure were examined using electron backscatter diffraction measurements in SEM (using a TESCAN MIRA3 microscope with a field emission gun) at the Michigan Center for Materials Characterization at the University of Michigan. After mechanical polishing, we acquired a scratch-free surface by FIB polishing using
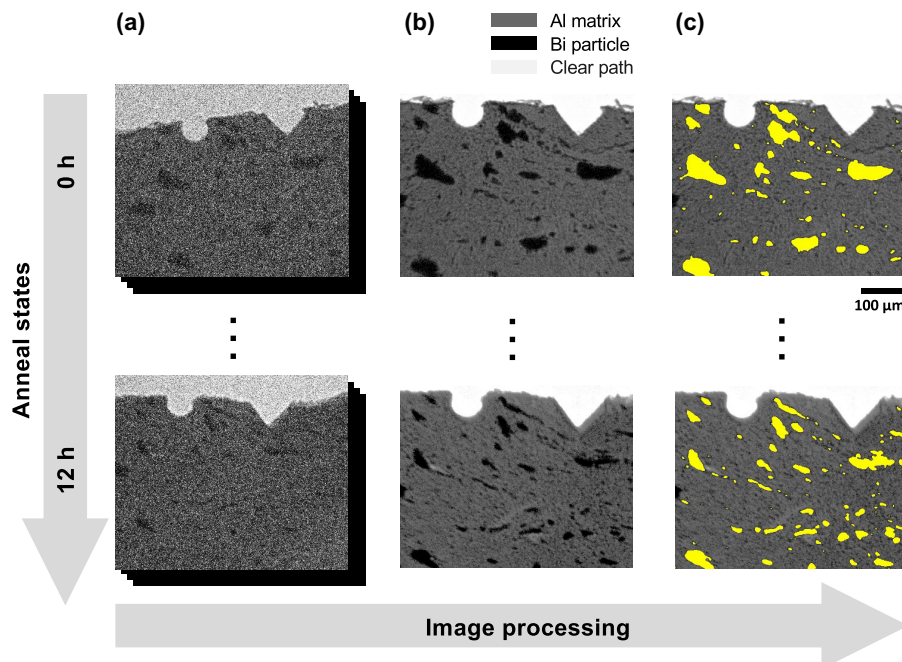

FIG. 7. Summary of the image processing procedures: (a) series of raw images at each annealing state, (b) after registration and normalization, and (c) segmentation of Bi particles.

the Helios G4 PFIB UXe dual-beam system. We analyzed the texture data with the aid of the MTEX toolbox [64] in MATLAB, to produce the results shown in Fig. 4.

APPENDIX E: CALCULATION OF SPATIAL RESOLUTION

Figure 8 shows a representative PSD profile that was averaged over multiple lines or traces in Fig. 7(b) to obtain a statistically representative result. Following the procedure given by Modregger *et al.* [40], we determine the value of the noise baseline, μ_s, as the mean value of the high-frequency components ($k > 2$ pixel^{-1}). The value of k_{res} is then found as 0.39 pixel^{-1} at the intersection between the power spectra and the $2\mu_s$ value. Accordingly, for a pixel size of 0.53 µm, the spatial resolution $x_{\text{res}} = 2\pi/k_{\text{res}} = 8.5$ µm.

APPENDIX F: CALCULATION OF GBW VELOCITY

According to the theory proposed by Glickman and Nathan [54], the wetting velocity Γ in the direction of the grain boundary trace at the root of a fingerlike groove is

$$\Gamma = \frac{(D_{\text{GB}}\gamma_{\text{GB}}m)^2\Omega}{D_L\gamma_{\text{SL}}C_{L\infty}L^2kT}. \tag{F1}$$

Here D_{GB} is the GB diffusivity, which follows an Arrhenius relation as $D_{\text{GB}} = D_{\text{GB}}^0 \exp(-\Delta H_{\text{GB}}/k_BT)$; γ_{GB} is the GB surface tension; Ω is the atomic volume of solid metal (Al); D_L is the diffusion coefficient of Al in liquid Bi; γ_{SL} is the solid-liquid interphase tension; $C_{L\infty}$ is the equilibrium solubility of Al in liquid Bi; L is the characteristic distance between dislocationlike defects that serve as sinks in the GB structure; and $m = 1 - [\cos(\theta_d/2)/\cos(\theta_0/2)]$, where θ_0 is the equilibrium dihedral angle and θ_d is the "dynamic"
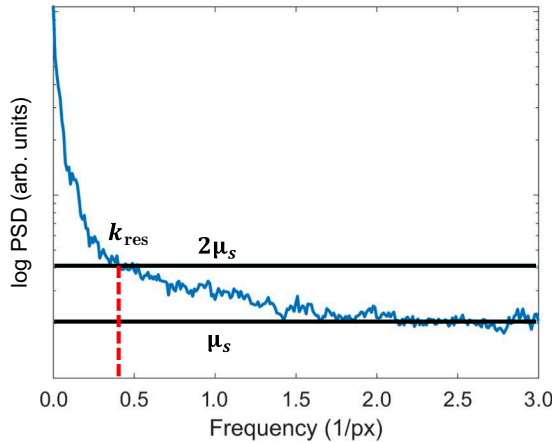

FIG. 8. Measurements of the spatial resolution by Fourier-based analysis of the PSD. An image of the sample at the 0 h mark [Fig. 2(a)] is used for the calculation.

TABLE I.   Parameters used in the calculation of the wetting velocity Γ.

Parameter	Value	Reference
D_{GB}^0 ($\times 10^5$ m^2/s)	1.89–1.94	[57,65]
ΔH_{GB} ($\times 10^5$ J/mol)	0.695–0.775	[57,65]
T (K)	553.15	
γ_{GB} (J/m^2)	0.34–0.35	[58,66]
D_L ($\times 10^{-9}$ m^2/s)	1.8	[67]
$\gamma_{\text{SL}} \cong 0.45\gamma_{\text{GB}}$ (J/m^2)	0.31–0.32	
Ω ($\times 10^{-29}$ m^3)	1.0	
$C_{L\infty}$	0.006	[68]
L ($\times 10^{-8}$ m)	8	[54]

dihedral angle [58]. The values of these parameters for the case of Al-Bi are given in Table I.

APPENDIX G: CONVERSION FROM MAJOR-AXIS TO MINOR-AXIS VELOCITY

In deriving Eq. (1) in the main text, we assume linear kinetics for the major axis of the particle [53,54],

$$v_{\text{major}} \propto 2\Gamma, \tag{G1}$$

where v_{major} represents its (constant) velocity, and Γ is determined by a collection of thermophysical parameters [Eq. (F1)]. As the liquid Bi pool is embedded inside the material, it is in contact with two fingerlike grooves opposite each other along the major axis (see inset of Fig. 2 and also Fig. 3). Thus, the pool lengthens along the major axis at twice the anticipated velocity for a single groove. Taking the liquid Bi pool to be in the shape of a three-dimensional spheroid, its volume Ω can be expressed as

$$\Omega = \frac{4\pi}{3}L_{\text{minor}}^2 L_{\text{major}}, \tag{G2}$$

where L_{minor} and c are the minor- and major-axis lengths, respectively. Then, given that Ω is conserved, we can relate the major-axis velocity $v_{\text{major}} \equiv (\partial L_{\text{major}}/\partial t)_\Omega$ to the minor-axis velocity $v_{\text{minor}} \equiv (\partial L_{\text{minor}}/\partial t)_\Omega$ as

$$
\begin{aligned}
v_{\text{minor}} &= \left(\frac{\partial L_{\text{minor}}}{\partial L_{\text{major}}}\right)_\Omega v_{\text{major}} \\
&= -2\Gamma\left(\frac{2\pi}{3\Omega}\right)L_{\text{minor}}^3 \\
&= -k_1 L_{\text{minor}}^3\Omega,
\end{aligned} \tag{G3}
$$

where we set $k_1 = 2\Gamma(2\pi/3\Omega)$. Integrating Eq. (G3) gives

$$L_{\text{minor}}(t) = (k_1 t + k_2)^{-1/2}, \tag{G4}$$

where k_2 is an integration constant.

At long times, Eq. (G4) predicts that $L_{\text{minor}}(t \to \infty) \to 0$ or conversely that $L_{\text{major}}(t \to \infty) \to \infty$ [Eq. (G2)]. Yet, it is more likely that the liquid pool would have pinched off via Rayleigh instability before thinning completely. That is, lengthening the pool (increasing c) raises the solid-liquid interfacial energy by increasing the ratio of surface area to volume of the liquid stream. To reduce this energy, the stream forms sinusoidal perturbations. As lengthening continues, the perturbations increase in amplitude until the stream subdivides into distinct, smaller pools. According to Rayleigh's criterion [47], the distance between the centers of mass of adjacent pools is directly proportional to the minor axis of the stream. Therefore, $L_{\text{minor}}(t \to \infty) > 0$ and a constant term, k_3, must be introduced into the general form [Eq. (G4)] to account for the finite size of the stream before it is rendered unstable; see again Eq. (1). We note that all three free parameters have a physical meaning: k_3 gives an (average) estimate of the critical wavelength of the morphological instability at long times; k_2 is set by the initial condition, $L_{\text{minor}}(t = 0) = k_2^{-1/2} + k_3$; and k_1 prescribes a rate for the GBW process.

———————

[1] R. Cunningham, C. Zhao, N. Parab, C. Kantzos, J. Pauza, K. Fezzaa, T. Sun, and A. D. Rollett, Keyhole threshold and morphology in laser melting revealed by ultrahigh-speed x-ray imaging, Science **363,** 849 (2019).

[2] C. Zhao, N. D. Parab, X. Li, K. Fezzaa, W. Tan, A. D. Rollett, and T. Sun, Critical instability at moving keyhole tip generates porosity in laser melting, Science **370,** 1080 (2020).

[3] L. Zhang, M. Sun, Q. Lv, C. F. Ukaomah, Q. Hu, B. Yu, J. Zhang, X. Liang, G. Wang, and S. Jiang, Evolution of shale microstructure under in situ heat treatment: Synchrotron small-angle X-ray scattering, Energy Fuels **35,** 4345 (2021).

[4] W. L. Tan, N. M. Kirby, Y.-B. Cheng, and C. R. McNeill, Origin of vertical slab orientation in blade-coated layered hybrid perovskite films revealed with in-situ synchrotron X-ray scattering, Nano Energy **83,** 105818 (2021).

[5] M. J. Higgins, J. Kang, G. Huang, D. Montiel, N. Lu, H. Liu, Y.-F. Shen, P. Staublin, J.-S. Park, J. D. Almer, P. Kenesei, P. G. Sanders, R. M. Suter, K. Thornton, and A. J. Shahani, Anomalous strain-energy-driven macroscale translation of grains during nonisothermal annealing, Phys. Rev. Mater. **5,** L070401 (2021).

[6] N. Lu, S. Moniri, M. R. Wiltse, J. Spielman, N. Senabulya, and A. J. Shahani, Dynamics of Ga penetration in textured Al polycrystal revealed through multimodal three-dimensional analysis, Acta. Mater **217,** 117145 (2021).

[7] X. Wu, H. Liu, and A. Yan, Phase-contrast X-ray tomography: Contrast mechanism and roles of phase retrieval, Eur. J. Radiol. **68,** S8 (2008).

[8] P. Cloetens, R. Barrett, J. Baruchel, J.-P. Guigay, and M. Schlenker, Phase objects in synchrotron radiation hard x-ray imaging, J. Phys. D: Appl. Phys. **29,** 133 (1996).

[9] A. Bhattacharya, Y.-F. Shen, C. M. Hefferan, S. F. Li, J. Lind, R. M. Suter, C. E. Krill, and G. S. Rohrer, Grain boundary velocity and curvature are not correlated in Ni polycrystals, Science **374,** 189 (2021).

[10] Z. Xu, Y.-F. Shen, S. K. Naghibzadeh, X. Peng, V. Muralikrishnan, S. Maddali, D. Menasche, A. R. Krause, K. Dayal, R. M. Suter, and G. S. Rohrer, Grain boundary migration in polycrystalline α-Fe, Acta Mater. **264,** 119541 (2024).

[11] Z. Ren, L. Gao, S. J. Clark, K. Fezzaa, P. Shevchenko, A. Choi, W. Everhart, A. D. Rollett, L. Chen, and T. Sun, Machine learning–aided real-time detection of keyhole pore generation in laser powder bed fusion, Science **379,** 89 (2023).

[12] X. Lei, Y. Zhang, J. Sun, F. Bachmann, X. Yang, R. E. Sanders, and D. Juul Jensen, Particle stimulated nucleation revisited in three dimensions: A laboratory-based multimodal X-ray tomography investigation, Mater. Res. Lett. **9,** 65 (2021).

[13] J. R. Schneider, R. Bouchard, T. Brückel, M. Lippert, H.-B. Neumann, H. F. Poulsen, U. Rütt, T. Schmidt, and M. von Zirnmermann, High energy synchrotron radiation. A new probe for condensed matter research, J. Phys. IV **04,** C9 (1994).

[14] B. Günther, R. Gradl, C. Jud, E. Eggl, J. Huang, S. Kulpe, K. Achterhold, B. Gleich, M. Dierolf, and F. Pfeiffer, The versatile X-ray beamline of the Munich Compact Light Source: Design, instrumentation and applications, J. Synchrotron Radiat. **27,** 1395 (2020).

[15] A. E. Hussein et al., Laser-wakefield accelerators for high-resolution X-ray imaging of complex microstructures, Sci. Rep. **9,** 3249 (2019).

[16] N. Lu, J. Kang, N. Senabulya, R. Keinan, N. Gueninchault, and A. J. Shahani, Dynamics of particle-assisted abnormal grain growth revealed through integrated three-dimensional microanalysis, Acta Mater. **195,** 1 (2020).

[17] D. H. Larsson, W. Vågberg, A. Yaroshenko, A. Ö. Yildirim, and H. M. Hertz, High-resolution short-exposure small-animal laboratory x-ray phase-contrast tomography, Sci. Rep. **6,** 39074 (2016).

[18] P. Bidola, K. Morgan, M. Willner, A. Fehringer, S. Allner, F. Prade, F. Pfeiffer, and K. Achterhold, Application of sensitive, high-resolution imaging at a commercial lab-based X-ray micro-CT system using propagation-based phase retrieval, J. Microsc. **266,** 211 (2017).

[19] N. Arai, T. Stan, S. Macfarland, P. W. Voorhees, N. S. Muyanja, A. J. Shahani, and K. T. Faber, Coarsening of dendrites in solution-based freeze-cast ceramic systems, Acta Mater. **215,** 117039 (2021).

[20] V. M. Segal, Materials processing by simple shear, Mater. Sci. Eng.: A **197,** 157 (1995).

[21] J. M. Cole et al., High-resolution μCT of a mouse embryo using a compact laser-driven X-ray betatron source, Proc. Natl. Acad. Sci. **115,** 6335 (2018).

[22] R. C. Shah, F. Albert, K. Ta Phuoc, O. Shevchenko, D. Boschetto, A. Pukhov, S. Kiselev, F. Burgy, J.-P. Rousseau, and A. Rousse, Coherence-based transverse measurement of synchrotron x-ray radiation from relativistic laser-plasma interaction and laser-accelerated electrons, Phys. Rev. E **74,** 045401(R) (2006).

[23] S. Kneip *et al.*, Bright spatially coherent synchrotron X-rays from a table-top source, Nat. Phys. **6**, 980 (2010).

[24] S. Kneip, C. McGuffey, F. Dollar, M. S. Bloom, V. Chvykov, G. Kalintchenko, K. Krushelnick, A. Maksimchuk, S. P. Mangles, T. Matsuoka, Z. Najmudin, C. A. Palmer, J. Schreiber, W. Schumaker, A. G. Thomas, and V. Yanovsky, X-ray phase contrast imaging of biological specimens with femtosecond pulses of betatron radiation from a compact laser plasma wakefield accelerator, Appl. Phys. Lett. **99**, 093701 (2011).

[25] M. Kozlova, I. Andriyash, J. Gautier, S. Sebban, S. Smartsev, N. Jourdain, U. Chaulagain, Y. Azamoum, A. Tafzi, J. P. Goddet, K. Oubrerie, C. Thaury, A. Rousse, and K. Ta Phuoc, Hard x rays from laser-wakefield accelerators in density tailored plasmas, Phys. Rev. X **10**, 011061 (2020).

[26] R. Rakowski, P. Zhang, K. Jensen, B. Kettle, T. Kawamoto, S. Banerjee, C. Fruhling, G. Golovin, D. Haden, M. S. Robinson, D. Umstadter, B. A. Shadwick, and M. Fuchs, Transverse oscillating bubble enhanced laser-driven betatron X-ray radiation generation, Sci. Rep. **12**, 10855 (2022).

[27] S. Fourmaux, E. Hallin, U. Chaulagain, S. Weber, and J. C. Kieffer, Laser-based synchrotron X-ray radiation experimental scaling, Opt. Express **28**, 3147 (2020).

[28] H. Zhang *et al.*, High-brightness betatron X-ray source driven by the SULF-1 PW laser, High Power Laser Sci. Eng. **13**, e31 (2025).

[29] F. Albert and A. G. R. Thomas, Applications of laser wakefield accelerator-based light sources, Plasma Phys. Controlled Fusion **58**, 103001 (2016).

[30] V. Senthilkumaran, N. F. Beier, S. Fourmaux, P. Shabaninezhad, J. Stinehart, L. Zhou, J. A. Moore, and A. E. Hussein, Laser-driven betatron x rays for high-throughput imaging of additively manufactured materials, Rev. Sci. Instrum. **95**, 123510 (2024).

[31] A. E. Bravo, H. A. Durán, V. H. Jacobo, A. Ortiz, and R. Schouwenaars, Towards new formulations for journal bearing alloys, Wear **302**, 1528 (2013).

[32] Z.-M. Wang, Q. Yang, Z.-P. Sun, B.-R. Zhang, W. Zhao, and W.-F. Rao, The effects of Bi and Pb on the soft phase in $Al_{82}Sn_{15}Si_{2.2}Cu_{0.8}$ sliding bearing alloy, Mater. Charact. **170**, 110684 (2020).

[33] L. Ratke and S. Diefenbach, Liquid immiscible alloys, Mater. Sci. Eng.: R: Rep. **15**, 263 (1995).

[34] K. Lepper, M. James, J. Chashechkina, and D. A. Rigney, Sliding behavior of selected aluminum alloys, Wear **203–204**, 46 (1997).

[35] B. Prinz, A. Romero, and L. Ratke, Casting process for hypermonotectic alloys under terrestrial conditions, J. Mater. Sci. **30**, 4715 (1995).

[36] M. Zha, Z.-Y. Yu, F. Qian, H.-Y. Wang, Y.-J. Li, R. H. Mathiesen, and H. J. Roven, Achieving dispersed fine soft Bi particles and grain refinement in a hypermonotectic Al–Bi alloy by severe plastic deformation and annealing, Scr. Mater. **155**, 124 (2018).

[37] J. M. García-Infanta, S. Swaminathan, A. P. Zhilyaev, F. Carreño, O. A. Ruano, and T. R. McNelley, Microstructural development during equal channel angular pressing of hypo-eutectic Al–Si casting alloy by different processing routes, Mater. Sci. Eng.: A **485**, 160 (2008).

[38] C. H. Su and P. W. Voorhees, The dynamics of precipitate evolution in elastically stressed solids—I. Inverse coarsening, Acta Mater. **44**, 1987 (1996).

[39] R. J. Shalloo *et al.*, Automation and control of laser wakefield accelerators using Bayesian optimization, Nat. Commun. **11**, 6355 (2020).

[40] P. Modregger, D. Lübbert, P. Schäfer, and R. Köhler, Spatial resolution in Bragg-magnified X-ray images as determined by Fourier analysis, Phys. Status Solidi A **204**, 2746 (2007).

[41] S. Corde, K. Ta Phuoc, G. Lambert, R. Fitour, V. Malka, A. Rousse, A. Beck, and E. Lefebvre, Femtosecond x rays from laser-plasma accelerators, Rev. Mod. Phys. **85**, 1 (2013).

[42] P. Willmott, in *An Introduction to Synchrotron Radiation* (John Wiley & Sons, Hoboken, New Jersey, USA, 2019), Chap. 8, pp. 367–402.

[43] *Synchrotron Radiation: Basics, Methods and Applications*, edited by S. Mobilio, F. Boscherini, and C. Meneghini (Springer, Berlin, Heidelberg, 2015).

[44] H. W. Kuhn, The Hungarian method for the assignment problem, Nav. Res. Logist. Q. **2**, 83 (1955).

[45] J. Munkres, Algorithms for the assignment and transportation problems, J. Soc. Ind. Appl. Math. **5**, 32 (1957).

[46] K. Riesen and H. Bunke, Approximate graph edit distance computation by means of bipartite graph matching, Image Vis. Comput. **27**, 950 (2009).

[47] R. Balluffi, S. Allen, and W. Carter, in *Kinetics of Materials* (John Wiley & Sons, Hoboken, New Jersey, USA, 2005), pp. 335–336.

[48] P. W. Voorhees, The theory of Ostwald ripening, J. Stat. Phys. **38**, 231 (1985).

[49] In the quasi-steady state, the critical size is of the same order of magnitude as the mean particle size (minor-axis length), $\langle L_{\text{minor}} \rangle$; according to the data presented in Fig. 2(a), $\langle L_{\text{minor}} \rangle \gg x_{\text{res}}$.

[50] H. J. Vogel and L. Ratke, Instability of grain boundary grooves due to equilibrium grain boundary diffusion, Acta Metall. Mater. **39**, 641 (1991).

[51] B. B. Straumal, W. Gust, and D. A. Molodov, Wetting transition on grain boundaries in Al contacting with a Sn-rich melt, Interface Sci. **3**, 127 (1995).

[52] B. Straumal, T. Muschik, W. Gust, and B. Predel, The wetting transition in high and low energy grain boundaries in the Cu(In) system, Acta Metall. Mater. **40**, 939 (1992).

[53] R. C. Hugo and R. G. Hoagland, In-situ TEM observation of aluminum embrittlement by liquid gallium, Scr. Mater. **38**, 523 (1998).

[54] E. E. Glickman and M. Nathan, On the kinetic mechanism of grain boundary wetting in metals, J. Appl. Phys. **85**, 3185 (1999).

[55] B. Straumal, E. Rabkin, W. Łojkowski, W. Gust, and L. S. Shvindlerman, Pressure influence on the grain boundary wetting phase transition in FeSi alloys, Acta Mater. **45**, 1931 (1997).

[56] The critical wavelength λ^* can be determined by finding the point of intersection between the curves $L_{\text{minor}}(t)$ (Fig. 3) and $L_{\text{major}}(t)/(2\sqrt{2}\,\pi)$, where $L_{\text{major}}(t)$ is the major-axis length of the Bi particle (not pictured). Note that L_{minor} and L_{major} are related under the assumption that the particle volume is conserved [see also Eq. (G2)].

[57] W. Gust, S. Mayer, A. Bögel, and B. Predel, Generalized representation of grain boundary self-diffusion data, J. Phys. Colloq. **46,** C4 (1985).

[58] G. Gottstein, D. Molodov, and L. Shvindlerman, in *Metals Process Simulation* (ASM International, Materials Park, Ohio, USA, 2010).

[59] D. Guénot, D. Gustas, A. Vernier, B. Beaurepaire, F. Böhle, M. Bocoum, M. Lozano, A. Jullien, R. Lopez-Martens, A. Lifschitz, and J. Faure, Relativistic electron beams driven by kHz single-cycle light pulses, Nat. Photonics **11,** 293 (2017).

[60] C. N. Danson *et al.*, Petawatt and exawatt class lasers worldwide, High Power Laser Sci. Eng. **7,** e54 (2019/ed).

[61] The data are available at https://doi.org/10.5281/zenodo.17359670.

[62] V. V. Stolyarov, Y. T. Zhu, I. V. Alexandrov, T. C. Lowe, and R. Z. Valiev, Influence of ECAP routes on the microstructure and properties of pure Ti, Mater. Sci. Eng.: A **299,** 59 (2001).

[63] P. Perona and J. Malik, Scale-space and edge detection using anisotropic diffusion, IEEE Trans. Pattern Anal. Mach. Intell. **12,** 629 (1990).

[64] F. Bachmann, R. Hielscher, and H. Schaeben, Texture analysis with MTEX—Free and open source software toolbox, Solid State Phenom. **160,** 63 (2010).

[65] A. M. Brown and M. F. Ashby, Correlations for diffusion constants, Acta Metall. **28,** 1085 (1980).

[66] T. Uesugi and K. Higashi, First-principles calculation of grain boundary energy and grain boundary excess free volume in aluminum: Role of grain boundary elastic energy, J. Mater. Sci. **46,** 4199 (2011).

[67] C. B. Porth and J. R. Cahoon, Interdiffusion of Bi in liquid Sn, J. Phase Equilib. Diffus. **31,** 149 (2010).

[68] Thermo-Calc Software TCAL6 Al-alloys database version 6.0.